47th AIAA Aerospace Sciences Meeting Including The New Horizons Forum and Aerospace Exposition
5 - 8 January 2009, Orlando, Florida

AIAA 2009-945

Comparison of High Order Schemes for Large Eddy Simulation of Circular Cylinder Flow

Yiqing Shen*, Gecheng Zha†
Dept. of Mechanical and Aerospace Engineering
Miami Wind ^{TM}
University of Miami
Coral Gables, Florida 33124
E-mail: yqshen@miami.edu, gzha@miami.edu

Abstract

This paper compares LES results of a cylinder flow with two sets of numerical schemes, two span lengths, and a coarse and refined mesh. One set of the numerical scheme is the 7th order WENO scheme for the inviscid fluxes and 6th order central differencing for the viscous terms (7-6), the other set is a 5th order WENO scheme with a 4th order central differencing(5-4). For this purpose, a fully conservative 6th-order central differencing for the viscous terms of compressible flows is developed. The new central differencing scheme uses the same stencil of the WENO scheme. No explicit subgrid scale models are used for the LES. The span length has a significant effect on the solution. The 5-4 scheme agrees better with the experiment with the span length of $1D$ and coarse mesh, whereas the 7-6 scheme performs better at the refined mesh with the span length of πD. However, both schemes have poorer results with the span length of πD.

1 Introduction

Large eddy simulation (LES) has been regarded as a viable engineering tool with rapidly enhanced computer architecture and mathematical modeling[1]. The presence of various regimes in the flow over a cylinder makes the computation of this flow an interesting and challenging task[2]. During the past decade, many large eddy simulations (LES) have been performed for subcritical Reynolds numbers, especially at $Re_D = 3900$, mainly due to the availability of the experimental results of Lourenco and Shih[3] and Ong and Wallace[4]. This flow has also been used as a benchmark case to examine theoretical issues pertaining to the application of LES in generalized curvilinear coordinate systems[5]. There is a general consensus that low-order upwind schemes are not able to predict correctly the base suction coefficient, separation angles and the size and structure of the recirculation zone behind the cylinder.

The two dominant subgrid-scale(SGS) models for LES are Smagorisky and dynamic subgrid-scale stress models. Boris et al.[6] was the first research group to take the numerical dissipation as the SGS model. For the flow over a circular cylinder, the large-eddy simulations with no subgrid scale model, or say, with implicit subgrid scale model, are also studied by Rizzetta et al.[7], Breuer[8], Park et al.[9], Kasliwal et

* Research Scientist, AIAA Member
† Associate Professor, AIAA Senior Member

al.[10]. A variety of discretization methods have been used, including spectral element method[11], B-spline method [2], third-order compact upwind-biased scheme and fourth-order compact scheme[9], sixth-order compact scheme [7], fifth- and seventh-order upwind difference schemes [12], FE/spectral algorithm[13], hybrid scheme of the upwind difference scheme and the second-order central difference scheme, QUICK, and fourth-order central difference scheme[8].

When the LES method with implicit subgrid scale model is used, the numerical dissipation of the adopted scheme should be able to produce the appropriate amount of SGS dissipation[14, 9]. Park et al [9] concluded that the numerical dissipation strongly affects large structures on resolved scales as well as unresolved turbulence, and it is difficult to assess the effect of numerical dissipation in a systematic manner since the numerical and physical parameters such as grid resolution, numerical dissipation and SGS dissipation are mixed up in a complex way. For the simulation of turbulent channel flows and jet flows, Meinke et al.[15] found that the use of a subgrid scale model does not improve the distributions of statistical variables. The results with AUSM and sixth-order compact scheme combined with compact filter show negligible difference. In Ref.[9], the static error analysis indicated that both the finite-differencing and aliasing errors increase as the amount of numerical dissipation increases. On the other hand, the dynamic error analysis led to nearly opposite conclusions in that the aliasing error decrease as the numerical dissipation increases and the finite-differencing error overwhelms the aliasing error.

The studies of Beaudan and Moin[12] and Mittal and Moin[16] show that the upwind schemes are not ideal candidates for LES because the numerical dissipation overwhelms the contribution from the SGS force. However, it is necessary to develop uniformly high-order nonoscillatory methods (e.g., ENO, WENO) when the problems contain strong discontinuity, such as the shock/boundary layer interaction and shock/vortex interaction flows.

Shen et al[17] studied the flow past a circular cylinder at $Re_D = 3900$ by using the 5th-order WENO scheme with a conservative 4th-order central differencing for viscous terms, and found that the spanwise length varied from D to πD affects the flowfield structure, especially on the mean crosswise velocity, and it results in different turbulent Reynolds stress. It is also observed in [17] by Shen et al that the Smagorisky SGS model yields little difference from the implicit LES model.

The purpose of this paper is to study the feasibility of a flux differencing splitting scheme for the inviscid fluxes with a 7th order WENO reconstruction for LES with no explicit subgrid scale model. To match the high order schemes for the inviscid fluxes, a fully conservative 6th-order central differencing scheme for viscous terms is suggested this paper. The central differencing scheme use the same WENO stencil so that the overall discretization can maintain the compactness and facilitate boundary condition treatment. The comparison with the results of 5th-order scheme for inviscid terms and 4th-order differencing for viscous terms is given to understand the effect of high order scheme on the LES with implicit subgrid scale models.

2 The Numerical Method

2.1 Governing Equations

The governing equations are the spatially filtered compressible Navier-Stokes equations. The spatial filtering removes the small scale high frequency components of the fluid motion, while keeping the unsteadiness associated with the large scale turbulent motion.

For an arbitrary function $u(x_i, t)$, the filtered variable $\bar{u}(x_i, t)$ is defined as:

$$\bar{u}(x_i, t) = \int_D G(x_i - \xi_i, \Delta) u(\xi_i, t) d\xi_i \tag{1}$$

where G is the filter function and Δ is the filter width and is associated with the mesh size.

Similar to the case of RANS, for compressible flows, it is convenient to introduce the Farve-filtered variable $\tilde{u}(x_i, t)$ as:

$$\tilde{u}(x_i, t) = \frac{\overline{\rho u}}{\bar{\rho}} \tag{2}$$

A variable can be thus decomposed into its Favre-filtered component and fluctuating component as:

$$u(x_i, t) = \tilde{u}(x_i, t) + u''(x_i, t) \tag{3}$$

Applying these definitions and following the derivation of Knight et al.[18], the filtered compressible Navier-Stokes equations in Cartesian coordinates can be expressed as:

$$\frac{\partial \mathbf{Q}}{\partial t} + \frac{\partial \mathbf{F}}{\partial x} + \frac{\partial \mathbf{G}}{\partial y} + \frac{\partial \mathbf{H}}{\partial z} = \frac{1}{Re}(\frac{\partial \mathbf{R}}{\partial x} + \frac{\partial \mathbf{S}}{\partial y} + \frac{\partial \mathbf{T}}{\partial z}) \tag{4}$$

where

$$\mathbf{Q} = \begin{pmatrix} \bar{\rho} \\ \bar{\rho}\tilde{u} \\ \bar{\rho}\tilde{v} \\ \bar{\rho}\tilde{w} \\ \bar{\rho}\tilde{e} \end{pmatrix}, \mathbf{F} = \begin{pmatrix} \bar{\rho}\tilde{u} \\ \bar{\rho}\tilde{u}^2 + \bar{p} \\ \bar{\rho}\tilde{u}\tilde{v} \\ \bar{\rho}\tilde{u}\tilde{w} \\ (\bar{\rho}\tilde{e} + \bar{p})\tilde{u} \end{pmatrix}, \mathbf{G} = \begin{pmatrix} \bar{\rho}\tilde{v} \\ \bar{\rho}\tilde{v}\tilde{u} \\ \bar{\rho}\tilde{v}^2 + \bar{p} \\ \bar{\rho}\tilde{v}\tilde{w} \\ (\bar{\rho}\tilde{e} + \bar{p})\tilde{v} \end{pmatrix}, \mathbf{H} = \begin{pmatrix} \bar{\rho}\tilde{w} \\ \bar{\rho}\tilde{w}\tilde{u} \\ \bar{\rho}\tilde{w}\tilde{v} \\ \bar{\rho}\tilde{w}^2 + \bar{p} \\ (\bar{\rho}\tilde{e} + \bar{p})\tilde{w} \end{pmatrix}$$

$$\mathbf{R} = \begin{pmatrix} 0 \\ \bar{\tau}_{xx} + \sigma_{xx} \\ \bar{\tau}_{xy} + \sigma_{xy} \\ \bar{\tau}_{xz} + \sigma_{xz} \\ Q_x \end{pmatrix}, \mathbf{S} = \begin{pmatrix} 0 \\ \bar{\tau}_{yx} + \sigma_{yx} \\ \bar{\tau}_{yy} + \sigma_{yy} \\ \bar{\tau}_{yz} + \sigma_{yz} \\ Q_y \end{pmatrix}, \mathbf{T} = \begin{pmatrix} 0 \\ \bar{\tau}_{zx} + \sigma_{zx} \\ \bar{\tau}_{zy} + \sigma_{zy} \\ \bar{\tau}_{zz} + \sigma_{zz} \\ Q_z \end{pmatrix},$$

The overbar denotes a regular filtered variable as given in eq. (1), and the tilde is used to denote the Favre filtered variable defined in eq. (2). In above equations, ρ is the density, u, v, w are the Cartesian velocity components in x, y, z directions, p is the static pressure, and e is the total energy per unit mass.

The $\bar{\tau}$ is the molecular viscous stress tensor and is estimated as:

$$\bar{\tau}_{ij} = \frac{2}{3}\tilde{\mu}\frac{\partial \tilde{u}_k}{\partial x}_k \delta_{ij} + \mu(\frac{\partial \tilde{u}_i}{\partial x_j} + \frac{\partial \tilde{u}_j}{\partial x_i}), \qquad i, j = 1, 2, 3 \tag{5}$$

The above equation is in the tensor form, where the subscript 1, 2, 3 represent the coordinates, x, y, z and the Einstein summation convention is used.

The molecular viscosity $\tilde{\mu} = \tilde{\mu}(\tilde{T})$ is determined by Sutherland law.

The σ is the subgrid scale stress tensor due to the filtering process and is expressed as:

$$\sigma_{ij} = -\bar{\rho}(\widetilde{u_i u_j} - \tilde{u}_i \tilde{u}_j) \tag{6}$$

The energy flux Q is expressed as:

$$Q_i = \tilde{u}_j(\bar{\tau}_{ij} + \sigma_{ij}) - \bar{q}_i + \Phi_i \tag{7}$$

where Φ is the subscale heat flux:

$$\Phi_i = -C_p\bar{\rho}(\widetilde{u_i T} - \tilde{u}_i \tilde{T}) \tag{8}$$

The $\bar{q}_i$ is the molecular heat flux:

$$\bar{q}_i = -\frac{\tilde{\mu}}{(\gamma-1)Pr}\frac{\partial a^2}{\partial x_i}$$

where $a = \sqrt{\gamma R\tilde{T}}$ is the speed of sound .

$$\bar{\rho}\tilde{e} = \frac{\bar{p}}{(\gamma-1)} + \frac{1}{2}\bar{\rho}(\tilde{u}^2 + \tilde{v}^2 + \tilde{w}^2) + \rho k \tag{9}$$

where γ is the ratio of specific heats, ρk is the subscale kinetic energy per unit volume.

$$\rho k = \frac{1}{2}\bar{\rho}(\widetilde{u_i u_i} - \tilde{u}_i\tilde{u}_i) = -\frac{1}{2}\sigma_{ii} \tag{10}$$

The closure of equation (4) requires a model for the subgrid scale stress σ_{ij} and heat flux Φ_{ij}. Following Refs.[6, 7, 8, 10], in this paper, the large-eddy simulations with no subgrid scale model, or say, with implicit subgrid scale model, is applied for the flow over a circular cylinder.

In the generalized coordinates, Eq.(4) can be written as:

$$\frac{\partial Q'}{\partial t} + \frac{\partial E'}{\partial \xi} + \frac{\partial F'}{\partial \eta} + \frac{\partial G'}{\partial \zeta} = \frac{1}{Re}\left(\frac{\partial R'}{\partial \xi} + \frac{\partial S'}{\partial \eta} + \frac{\partial T'}{\partial \zeta}\right) \tag{11}$$

where,

$$Q' = \frac{1}{J}Q,$$
$$E' = \frac{1}{J}(\xi_t U + \xi_x E + \xi_y F + \xi_z G),$$
$$F' = \frac{1}{J}(\eta_t U + \eta_x E + \eta_y F + \eta_z G),$$
$$G' = \frac{1}{J}(\zeta_t U + \zeta_x E + \zeta_y F + \zeta_z G),$$
$$R' = \frac{1}{J}(\xi_x R + \xi_y S + \xi_z T),$$
$$S' = \frac{1}{J}(\eta_x R + \eta_y S + \eta_z T),$$
$$T' = \frac{1}{J}(\zeta_x R + \zeta_y S + \zeta_z T).$$

For simplicity, the prime $'$ in Eq.(11) will be omitted.

The spatially filtered Navier-Stokes equation [Eq. (11)] is solved by the fully conservative high order schemes given in the following section.

3 Spatial Discretization Schemes

3.1 Flux Difference Splitting and High Order Reconstruction

The Roe's flux difference scheme [19] is used as the Riemann solver with a 7th order WENO-type scheme in this paper. For the rest of the paper, we will take the flux in ξ direction as the example to explain the numerical methodology. Other directions can be obtained following the symmetric rule.

For the Roe scheme,

$$E_{i+\frac{1}{2}} = \frac{1}{2}[E(Q^L) + E(Q^R) - \tilde{A}(Q^R - Q^L)]_{i+\frac{1}{2}} \tag{12}$$

where

$$\tilde{A} = M|\Lambda|M^{-1}$$

Λ is the diagonal eigenvalue matrix,

$$\Lambda = diag(U, U, U, U + C, U - C)$$

where

$$U = \xi_x u + \xi_y v + \xi_z w$$
$$C = c\sqrt{\xi_x^2 + \xi_y^2 + \xi_z^2}$$

The high order accuracy of $E_{i+1/2}$ is obtained by achieving the high order accuracy of the left and right conservative variables Q^L and Q^R using the high order reconstruction. This procedure is similar to the MUSCL scheme suggested by van Leer[20].

For a variable u^L, the WENO reconstructions[21, 22] can be written as:

$$u^L_{i+\frac{1}{2}} = \sum_{k=0}^{r-1} \omega_k q_k(u_{j+k-r+1}, u_{j+k-r+2}, \cdots, u_{j+k}) \tag{13}$$

The weight ω_k is defined as

$$\omega_k = \frac{\alpha_k}{\alpha_0 + \cdots + \alpha_{r-1}},$$

where

$$\alpha_k = \frac{C_k}{(\epsilon + IS_k)^p}, k = 0, 1, \cdots, r-1 \tag{14}$$

where ϵ is a small positive real number introduced to avoid the denominator becoming zero; C_k are the optimal weight coefficients. IS_k is the smoothness measurement of the flux function on the kth candidate stencil.

For the computation of the cylinder flow in this paper with no shock discontinuities, the WENO scheme is disabled so that ω_k are equal to the optimal C_k to achieve the minimum numerical dissipation.

For $r = 4$, we have:

$$\begin{aligned}
q_0 &= -\tfrac{1}{4}u_{i-3} + \tfrac{13}{12}u_{i-2} - \tfrac{23}{12}u_{i-1} + \tfrac{25}{12}u_i \\
q_1 &= \tfrac{1}{12}u_{i-2} - \tfrac{5}{12}u_{i-1} + \tfrac{13}{12}u_i + \tfrac{1}{4}u_{i+1} \\
q_2 &= -\tfrac{1}{12}u_{i-1} + \tfrac{7}{12}u_i + \tfrac{7}{12}u_{i+1} - \tfrac{1}{12}u_{i+2} \\
q_3 &= \tfrac{1}{4}u_i + \tfrac{13}{12}u_{i+1} - \tfrac{5}{12}u_{i+2} + \tfrac{1}{12}u_{i+3}
\end{aligned} \tag{15}$$

$$C_0 = \frac{1}{35}, C_1 = \frac{12}{35}, C_2 = \frac{18}{35}, C_3 = \frac{4}{35} \tag{16}$$

Based on Eq. (13) with $\omega_k = C_k$, the 7th-order accuracy reconstruction is obtained as:

$$u^L_{i+1/2} = -\frac{1}{140}u_{i-3} + \frac{5}{84}u_{i-2} - \frac{101}{420}u_{i-1} + \frac{319}{420}u_i + \frac{107}{210}u_{i+1} - \frac{19}{210}u_{i+2} + \frac{1}{105}u_{i+3} \tag{17}$$

The u^R is constructed symmetrically as u^L about $i + 1/2$.

3.2 The 6-Order Finite Differencing Scheme for Viscous Terms

A fully conservative sixth-order accurate finite central differencing scheme for the viscous terms is derived below with the constraint that the stencil width should not be greater than that of the 7th order WENO scheme. This is important to maintain the compactness of the overall discretization schemes and facilitate boundary condition treatment.

For example,

$$\frac{\partial R}{\partial \xi}|_i = \frac{1}{\Delta \xi}(\tilde{R}_{i+1/2} - \tilde{R}_{i-1/2}) \tag{18}$$

where

$$\tilde{R}_{i-1/2} = \frac{1}{1920}(9R_{i+3/2} - 116R_{i+1/2} + 2134R_{i-1/2} - 116R_{i-3/2} + 9R_{i-5/2}) \tag{19}$$

$$R = [(\xi_x \tau_{xx}) + (\eta_y \tau_{xy}) + (\zeta_z \tau_{xz})]$$

$$\begin{aligned}(\tau_{xx}) = \quad & \mu\{\tfrac{4}{3}\left[(\xi_x \tfrac{\partial u}{\partial \xi}) + (\eta_x \tfrac{\partial u}{\partial \eta}) + (\zeta_x \tfrac{\partial u}{\partial \zeta})\right] \\ & -\tfrac{2}{3}[(\xi_y \tfrac{\partial v}{\partial \xi}) + (\eta_y \tfrac{\partial v}{\partial \eta}) + (\zeta_y \tfrac{\partial v}{\partial \zeta}) \\ & (\xi_z \tfrac{\partial w}{\partial \xi}) + (\eta_z \tfrac{\partial w}{\partial \eta}) + (\zeta_z \tfrac{\partial w}{\partial \zeta})]\}\end{aligned} \tag{20}$$

If R in Eq.(19) can be approximated with the accuracy order not lower than 6th order, the Taylor series expansion analysis of (18) and (19) will give

$$\frac{1}{\Delta \xi}(\tilde{R}_{i+1/2} - \tilde{R}_{i-1/2}) = R^{'}(\xi_i) + O(\Delta \xi^6) \tag{21}$$

Hence, the 6th order accuracy is achieved. It needs to point out that in Eq. (18), $\tilde{R}_{i+1/2}$ can not be replaced by $R_{i+1/2}$. Otherwise, the 6th order accuracy can not be achieved even though the high order approximation of $R_{i+1/2}$ is used. The 6th order accuracy from Eq. (18)-(21) is also based on the condition that the grid is uniform with $\Delta \xi = C$ in the generalized coordinates.

In order to achieve the highest order accuracy of R_I ($I = i - 5/2, i - 3/2, i - 1/2, i + 1/2, i + 3/2$) in a stencil not wider than the 7th order WENO stencil, for example, the stencil $S = (x_{i+r}, x_{i+r+1}, \cdots, x_{i+s})$ for all $\frac{\partial u}{\partial \eta}|_I$, $I = i - 5/2, i - 3/2, i - 1/2, i + 1/2, i + 3/2$, we give the following formulas,

$$\mu_I = \sum_{l=m}^{n} C_l^I \mu_{i+l}, \ m = -3, n = 2, \tag{22}$$

$$\frac{\partial u}{\partial \xi}|_I = \frac{1}{\Delta \xi} \sum_{l=r}^{s} D_l^I u_{i+l}, \ r = -4, s = 3, \tag{23}$$

$$\frac{\partial u}{\partial \eta}|_I = \sum_{l=m}^{n} C_l^I \frac{\partial u}{\partial \eta}|_{i+l,j}, \ m = -3, n = 2, \tag{24}$$

where

$$\frac{\partial u}{\partial \eta}|_{i,j} = \frac{1}{\Delta \eta} \sum_{l=p}^{q} C_l^c u_{i,j+l}, \ p = -3, q = 3, \tag{25}$$

The other terms are determined similarly.

By choosing different ranges for $(m, n), (r, s), (p, q)$ and different coefficients C_l^I, D_l^I, C_l^c, one can obtain the different order accuracy of the viscous terms. The principle of choosing $(m, n), (r, s), (p, q)$ is

to ensure that the approximation of $\frac{\partial R}{\partial \xi}|_i$ Eq. (18) is a central differencing. In this paper, we take $(m,n) = (-3,2), (r,s) = (-4,3), and\ (p,q) = (-3,3)$, and the coefficients C_l^I, D_l^I, C_l^c are given in Tables 1-3.

Taylor's series expansion analysis of (22)-(25) show that $\mu_I, \frac{\partial u}{\partial \eta}|_I, \frac{\partial u}{\partial \eta}|_{i,j}$ achieves sixth-order accuracy, and $\frac{\partial u}{\partial \xi}|_I$ achieve seventh-order accuracy.

Table 1: The coefficients of C_l^I

I	C_{-3}^I	C_{-2}^I	C_{-1}^I	C_0^I	C_1^I	C_2^I
$i-5/2$	63/256	315/256	-105/128	63/128	-45/256	7/256
$i-3/2$	-7/256	105/256	105/128	-35/128	21/256	-3/256
$i-1/2$	3/256	-25/256	75/128	75/128	-25/256	3/256
$i+1/2$	-3/256	21/256	-35/128	105/128	105/256	-7/256
$i+3/2$	7/256	-45/256	63/128	-105/128	315/256	63/256

Table 2: The coefficients of D_l^I

I	D_{-4}^I	D_{-3}^I	D_{-2}^I	D_{-1}^I	D_0^I	D_1^I	D_2^I	D_3^I
$i-5/2$	3043/107520	-5353/5120	4731/5120	733/3072	-239/1024	597/5120	-167/5120	143/35840
$i-3/2$	-143/35840	185/3072	-1185/1024	1175/1024	-125/3072	-51/5120	5/1024	-5/7168
$i-1/2$	5/7168	-49/5120	245/3072	-1225/1024	1225/1024	-245/3072	49/5120	-5/7168
$i+1/2$	5/7168	-5/1024	51/5120	125/3072	-1175/1024	1185/1024	-185/3072	143/35840
$i+3/2$	-143/35840	167/5120	-597/5120	239/1024	-733/3072	-4731/5120	5353/5120	-3043/107520

Table 3: The coefficients of C_l^c

C_{-3}^c	C_{-2}^c	C_{-1}^c	C_0^c	C_1^c	C_2^c	C_3^c
-1/60	3/20	-3/4	0	3/4	-3/20	1/60

Note that, even though the coefficients given in Table 1-3 may not be symmetric about the interface, the central differencing is achieved when they are substituted into Eq. (18).

4 Time Discretization

A pseudo temporal term $\frac{\partial Q}{\partial \tau}$ is added to the governing equation (4) for unsteady computations. The temporal term $\frac{\partial Q}{\partial t}$ is discretized implicitly using a 2nd-order three point, backward differencing as the following

$$\frac{\partial Q}{\partial t} = \frac{3Q^{n+1} - 4Q^n + Q^{n-1}}{2\Delta t},$$

and the pseudo temporal term is discretized with first-order Euler scheme to enhance diagonal dominance. The semi-discretized governing equation (4) can then be expressed as

$$[(\frac{1}{\Delta\tau} + \frac{1.5}{\Delta t})I - (\frac{\partial R}{\partial Q})^{n+1,m}]\delta Q^{n+1,m+1} = R^{n+1,m} - \frac{3Q^{n+1,m} - 4Q^n + Q^{n-1}}{2\Delta t}, \tag{26}$$

where n is the physical time level index, m is the iteration index within a physical time step, Δt and $\Delta\tau$ are the physical and pseudo time step, R is the net flux of the discretized spatial terms of Eq.

(11) using the scheme from section 3.1-3.2. Eq. (26) is solved using the unfactored Gauss-Seidel line iteration[23].

4.1 The Boundary Conditions

Steady state freestream conditions are used for the upstream portion of the outer boundary. For downstream boundary, the static pressure was specified as freestream value, and the streamwise gradients of other variables were forced to vanish. The periodic boundary condition is used in spanwise direction. The wall treatment suggested in [24] to achieve the flux conservation by shifting half interval of the mesh on the wall is employed. The no slip condition is employed on the cylinder surface, for computing the flux $F_{1/2}$ on the wall, there is

$$G_w = \begin{bmatrix} \rho V \\ \rho u V + p\eta_x \\ \rho v V + p\eta_y \\ \rho w V + p\eta_z \\ (\rho e + p)V \end{bmatrix}_w = \begin{bmatrix} 0 \\ p\eta_x \\ p\eta_y \\ p\eta_z \\ 0 \end{bmatrix}_w$$

and a third-order accuracy wall boundary formula is used to evaluate $p|_w$,

$$p_w = \frac{1}{6}(11p_1 - 7p_2 + 2p_3)$$

5 Results and Discussion

5.1 Flow Past a Circular Cylinder with $Re = 3900$

The turbulent flow passing a circular cylinder at Mach number of 0.2 and Reynolds number of 3900 is simulated in this paper to investigate the effect of numerical schemes, mesh size, and span length.

Two sets of the spatial discretization schemes are used: 1) 7th order Riemann solver with 6th order central differencing (7-6) as described in this paper; 2) 5th order Riemann solver with 4th order central differencing (5-4) as described in Ref.[24].

Two span lengths are used, D and πD, where D is the cylinder diameter. Two sets of O-type grid are used. The baseline mesh is for the span length of D with the mesh size of $120 \times 80 \times 30$ in the azimuthal, radial and spanwise directions in the physical domain of $\pi D \times 75D \times D$. The refined mesh is for the span length of πD with the mesh size of $240 \times 160 \times 180$ and the physical domain of $\pi D \times 75D \times \pi D$. Same as in Ref. [10], the first grid-point non-dimensional spacing of 7.7×10^{-5} is used. Fig.1 gives the grid sketch of $x - y$ plane close to the cylinder surface.

The uniform initial flowfield is used to start the simulation and the transition period is up to dimensionless time $t = 100$. Then the statistical results are obtained from $t = 100$ to $t = 250$. Within each physical time step, 20 pseudo time steps are used with the L_2 Norm residual reduced by $3 - 4$ order of magnitude.

The mean pressure coefficient compared with the experiment along the surface of the cylinder is given in Fig. 2. Fig. 2(a) is the result of mesh $120 \times 80 \times 30$ for spanwise length (SL) of $1D$. In the region of about $\theta < 55^o$, the mean pressure coefficient computed by both schemes agree well with experiment. In the region of about $\theta > 55^o$, the 7-6 scheme predicts the suction peak pressure lower than the experiment. The 5-4 scheme results agrees better with the experiment. Fig. 2(a)

shows that, for $SL = \pi D$, the simulated pressure coefficients are larger than experiments. For the case, the 7-6 scheme agree better with the experiment than the 5-4 scheme.

Fig. 3 shows the mean streamwise velocity on the centerline in the wake of the cylinder. The results with $SL = 1D$ are closer to the experiment. But for $SL = \pi D$, the 7-6 scheme is better than the 5-4 scheme.

Figs. 4 and 5 give the distributions of the mean streamwise velocity and the mean crossflow velocity for three streamwise locations, $x/D = 1.06, x/D = 1.54$ and $x/D = 2.02$. For the case of $SL = 1D$, they are in good agreement with the results computed by the other two groups[2, 10], except that the depth of the wake predicted is a little shallow. The velocity filed is changed when SL increased from $1D$ to πD. This indicates the spanwise length affects the flow filed structure behind the cylinder.

The streamwise, shear and lateral Reynolds stress are given in Figs. 6-8. It can be seen that the results of 5-4 agree with experiment better than the scheme 7-6 with $SL = 1D$. Both two results are better than the results computed by Rizzetta et al[7], in which the 6th-order compact scheme with a high order filter and a finer mesh size of $199 \times 197 \times 53$ are used. With $SL = \pi D$, the results of the 7-6 scheme are more similar to Rizzetta's results.

Figs. 9-10 are the instantaneous vorticity contours at $t = 250T$. It can be seen that, near the cylinder, the results obtained by the 7-6 scheme contains more small-scale structure than the lower order scheme. And the region containing small-scale structure is also longer. Comparing the results of $SL = 1D$ and $SL = \pi D$, it can be found the similar phenomenon that the flowfiled of larger SL contains more small-scale structure and longer vortex shedding region. Further downstream of the cylinder, the large vorticity structure of higher order scheme decays faster than the lower order scheme and the wake spread angle of the 7-6 scheme is narrower than that of the 5-4 scheme. The difference of the small-scale structure region resolved by the different span length and mesh size results in the difference of the cylinder surface pressure distribution and the velocity distribution behind the cylinder as shown in Fig. 2 and 3.

For $SL = 1D$ with the coarse baseline mesh, it appears that the results of both the 5-4 scheme and the 7-6 scheme agree well with experiments. The results of the 5-4 scheme are closer to the experiment, in particular for the Reynolds stresses. For the $SL = \pi D$ with the refined mesh, the results of both the schemes are more deviated from the experiment with the results of the 7-6 scheme closer to the experiment and the LES results of Rizzetta et al[7].

The reasons for above outcome are not clear. First, the detailed experiment setup is not available and it is not clear what the span length was used in the experiment and what is the span length effect on the measured results in the experiment. Second, the 5-6 scheme performs better than the 7-6 scheme on the coarse mesh with the span length of D may be related to the recent finding that a higher order scheme may have poorer accuracy than a lower order scheme on a coarse mesh[25].

6 Conclusion

This paper compares LES results of a cylinder flow with two sets of numerical schemes, two span lengths, and a coarse and refined mesh. One set of the numerical scheme is the 7th order WENO scheme for the inviscid fluxes and 6th order central differencing for the viscous terms (7-6), the other set is a 5th order WENO scheme with a 4th order central differencing(5-4). For this purpose, a fully conservative 6th-order central differencing for the viscous terms of compressible flows is developed. The new central differencing scheme uses the same stencil of the WENO scheme. No explicit subgrid scale models are used for the LES. For the span length of $1D$ with the coarse

baseline mesh, the results of both the 5-4 scheme and the 7-6 scheme agree well with experiments. The results of the 5-4 scheme are closer to the experiment, in particular for the Reynolds stresses. For the span length of πD with the refined mesh, the results of both the schemes are more deviated from the experiment with the results of the 7-6 scheme closer to the experiment and the LES results of Rizzetta et al. The span length has a significant effect on the simulation for the overall solutions including length of vortex shedding region, wake spread angle, Reynolds stresses, mean flow results, and small vortex structures. The detailed experiment setup is not available and it is not clear what the span length was used in the experiment and what is the span length effect on the measured results in the experiment. The 5-6 scheme performs better than the 7-6 scheme on the coarse mesh with the span length of D may be related to the recent finding that a higher order scheme may have poorer accuracy than a lower order scheme on a coarse mesh.

7 Acknowledgment

This work is partially supported by ARO/AFOSR Grant 50827-RT-ISP and by Miami Wind ^{TM} at University of Miami.

References

[1] P. Moin, "Advances in large eddy simulation methodology for complex flows," *Int.J.Heat Fluid Flow*, vol. 23, p. 710, 2002.

[2] G. Kravchenko, P. Moin , " Numerical studies of flow over a circular cylinder at $Re_D = 3900$," *Phys.Fluids* , vol. 12, pp. 403–417, 2000.

[3] L.M. Lourenco, C. Shih , " Characteristics of the plane turbulent near wake of a circular cylinder, A particle image velocity study ." private communication by Beaudan and Moin (data taken from[**?**]), 1993.

[4] L. Ong, J. Wallace , " The velocity field of the turbulent very near wake of a circular cylinder ," *Exp.Fluids* , vol. 20, p. 441, 1996.

[5] Chunlei Liang, George Papadakis , " Large eddy simulation of pulsating flow over a circular cylinder at subcritical Reynolds number ," *Computer& Fluids* , vol. 36, pp. 299–312, 2007.

[6] J. Boris, F. Grinstein, E. Oran, and R. Kolbe, "New Insights into Large Eddy Simulation," *Journal of Fluid Mechanics*, vol. 41, pp. 453–480, 1970.

[7] D.P. Rizzetta, M.R. Visbal, G.A. Blaisdell, " A time-implicit high-order compact differencing and flitering scheme for Large-eddy simulation ," *Int.J.Numer.Meth.Fluids* , vol. 42, pp. 665–693, 2003.

[8] M. Breuer , " Numerical and modeling influences on large eddy simulations for the flow past a circular cylinder ," *Int.J.Heat Fluid Flow* , vol. 19, p. 512, 1998.

[9] Noma Park, Jung Yul Yoo, Haecheon Choi , " Discretization errors in large eddy simulation: on the suitability of centered and upwind-biased compact difference schemes ," *J.Comput.Phys.* , vol. 198, pp. 580–616, 2004.

[10] A. Kasliwal, K. Ghia, U. Ghia , " Higher-order accurate solution for flow past a circular cylinder at $Re = 13,4000$." AIAA-2005-1123, 43rd AIAA Aerospace Sciences Meeting and Exhibit, Reno, Nevada,10-13 Jan., 2005.

[11] H.M. Blackburn, S. Schmidt , " Large eddy simulation of flow past a circular cylinder ." 14th Australasian Fluid Mechanics Conference, Adelaide University, Adelaide, Australia, 10-14 Dec, 2001.

[12] P. Beaudan, P. Moin , " Numerical experiments on the flow past a circular cylinder at a sub-critical Reynolds number ." Report No.TF-62, Department of Mechanical Engineering, Stanford University, 1994.

[13] D.O. Snyder, G. Degrez, " Large-eddy simulation with complex 2-D geometries using a parallel finite-enement/spetral algorithm ," *Int.J.Numer.Meth.Fluids* , vol. 41, pp. 1119–1135, 2003.

[14] E. Garnier, M. Mossi, P. Sagaut, P. Comte, M. Deville , " On the use of shock-capturing schemes for large-eddy simulation ," *J.Comput.Phys.* , vol. 153, pp. 273–311, 1999.

[15] M. Meinke, W. Schroder, E. Krause, Th. Rister, "A comparison of second- and sixth-order methods for large-eddy simulations," *Computers & Fluids*, vol. 31, pp. 695–718, 2002.

[16] R. Mittal and P. Moin, "Suitability of Upwind-Biased Schemes for Large-Eddy Simulation of Turbulent Flows," *AIAA Journal*, vol. 36, pp. 1415–1417, 1997.

[17] Y. Q. Shen, G. -C. Zha, B. Y. Wang, "Large Eddy Simulation of Circular Cylinder Flow by Using High Order WENO Scheme." AIAA Paper 2008-3748, AIAA 38th Fluid Dynamics Conference and Exhibit, Seattle, Washington, Jun 2008.

[18] D. Knight, G. Zhou, N. Okong'o, and V. Shukla, "Compressible Large Eddy Simulation Using Unstructured Grids." AIAA Paper 98-0535, 1998.

[19] P. Roe, "Approximate Riemann Solvers, Parameter Vectors, and Difference Schemes," *Journal of Computational Physics*, vol. 43, pp. 357–372, 1981.

[20] B. Van Leer, "Towards the Ultimate Conservative Difference Scheme, III," *Journal of Computational Physics*, vol. 23, pp. 263–75, 1977.

[21] G.S. Jiang, and C.W. Shu, "Efficient implementation of weighted ENO schemes," *J.Comput.Phys.*, vol. 126, pp. 202–228, 1996.

[22] D.S. Balsara and C.-W. Shu, "Monotonicity Preserving weighted essentially non-oscillatory schemes with increasingly high order of accuracy," *J.Comput.Phys.*, vol. 160, pp. 405–452, 2000.

[23] Y.Q. Shen, B.Y. Wang,and G.C. Zha, "Comparison Study of Implicit Gauss-Seidel Line Iteration Method for Transonic Flows." AIAA-paper 2007-4332, June 2007.

[24] Y.Q. Shen, B.Y. Wang,and G.C. Zha, "Implicit WENO scheme and high order viscous formulas for compressible flows." AIAA-paper 2007-4431, June 2007, to appear in AIAA Journal.

[25] Y. Q. Shen, G. -C. Zha, "High Order Finite Differencing Schemes and Their Accuracy for CFD." AIAA Paper 2009-1137, 47th AIAA Aerospace Sciences Meeting, Orlando, FL, Jan 5-8, 2009.

[26] C. Norberg , " Effects of Reynolds number, low-intensity free-stream turbulence on the flow around a circular cylinder ." Publ.No.87/2,Department of Applied Themoscience and Fluid Mechanics, Chalmer University of Technology, Gothenberg, Sweden, 1987.

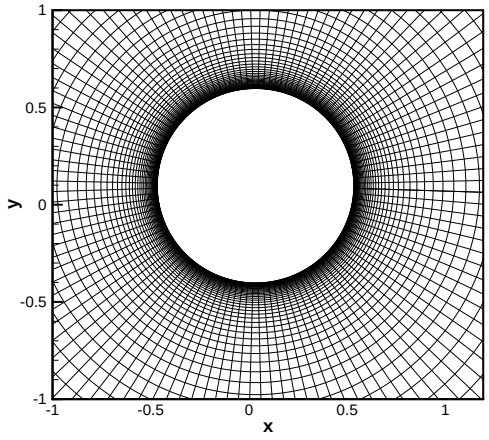

Figure 1: Sketch of mesh in $x - y$ plane

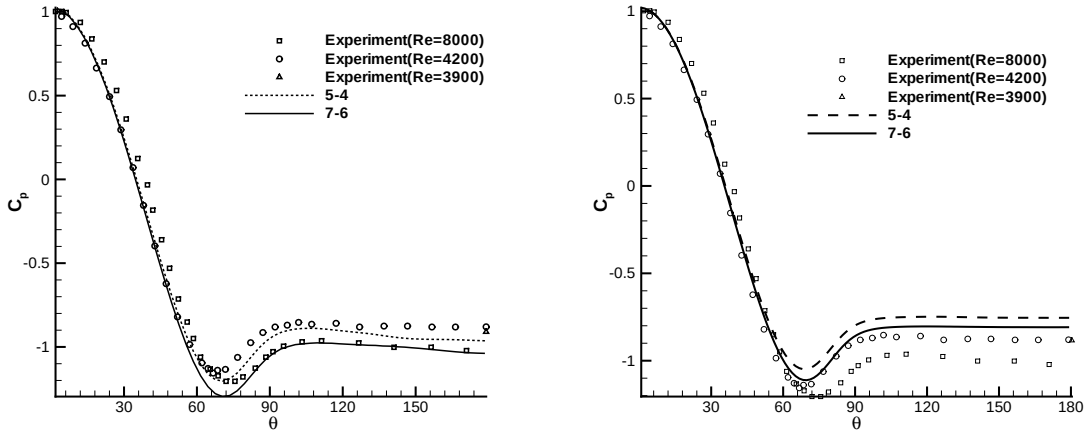

a. $1D$, $120 \times 80 \times 30$ b. πD, $240 \times 160 \times 180$

Figure 2: Mean pressure coefficient variation on the surface of the cylinder. Experiment is from Norberg[26]

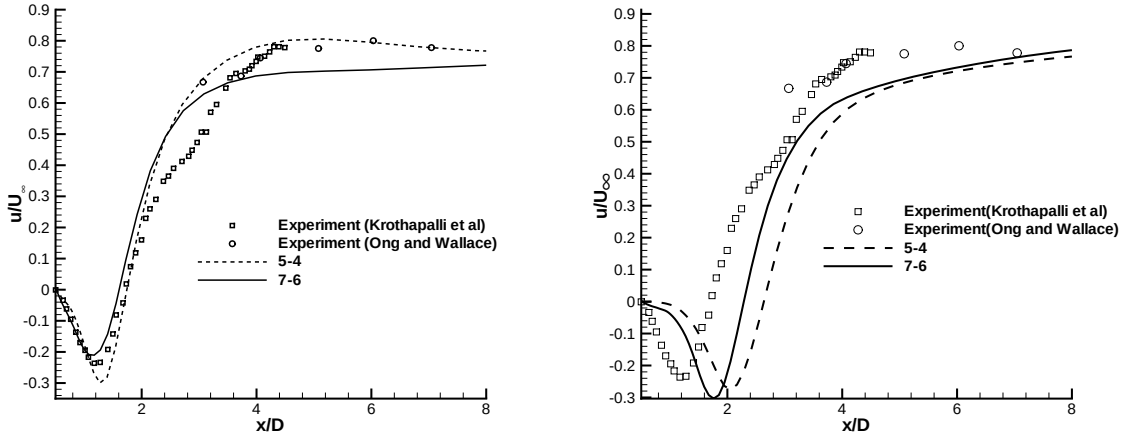

a. $1D$, $120 \times 80 \times 30$ b. πD, $240 \times 160 \times 180$

Figure 3: Mean streamwise velocity on the centerline in the wake of the cylinder

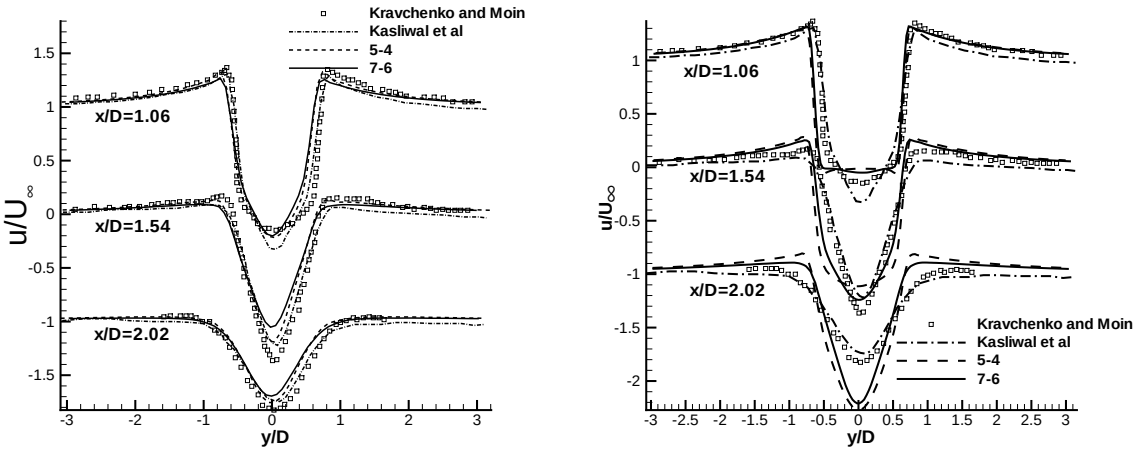

a. $1D$, $120 \times 80 \times 30$ b. πD, $240 \times 160 \times 180$

Figure 4: Mean streamwise velocity profiles at 3 locations in the wake of the cylinder

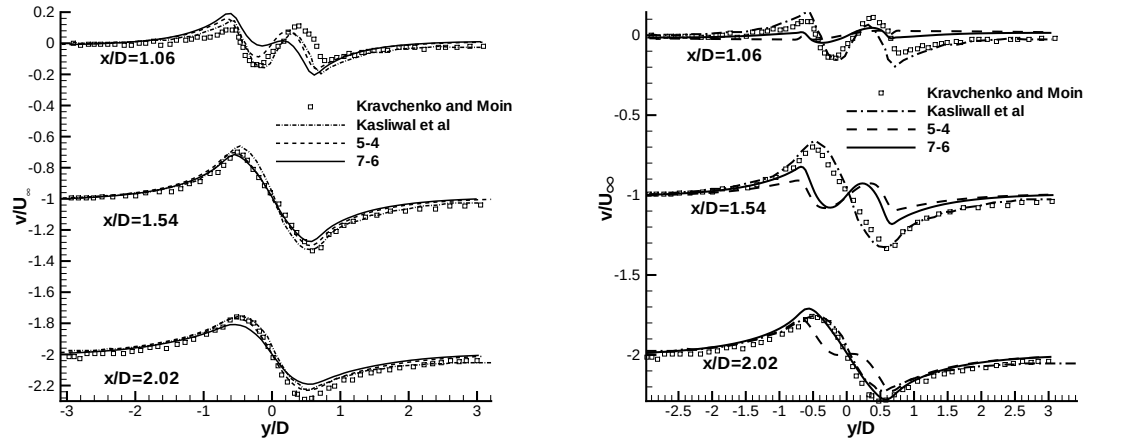

a. $1D$, $120 \times 80 \times 30$ b. πD, $240 \times 160 \times 180$

Figure 5: Mean crossflow velocity profiles at 3 locations in the wake of the cylinder

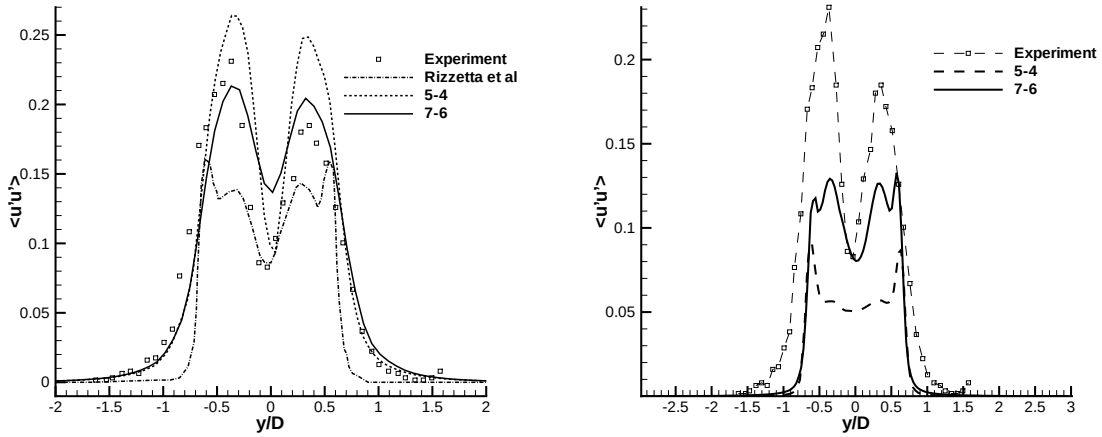

a. $1D$, $120 \times 80 \times 30$ b. πD, $240 \times 160 \times 180$

Figure 6: Streamwise Reynolds Stress in the wake at $x/D = 1.54$ Plane

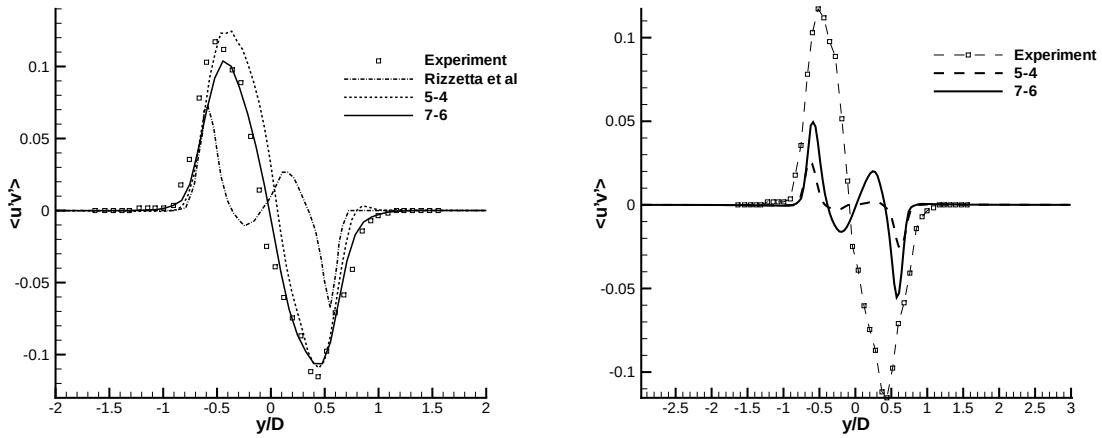

a. $1D$, $120 \times 80 \times 30$ b. πD, $240 \times 160 \times 180$

Figure 7: Shear Reynolds Stress in the wake at $x/D = 1.54$ Plane

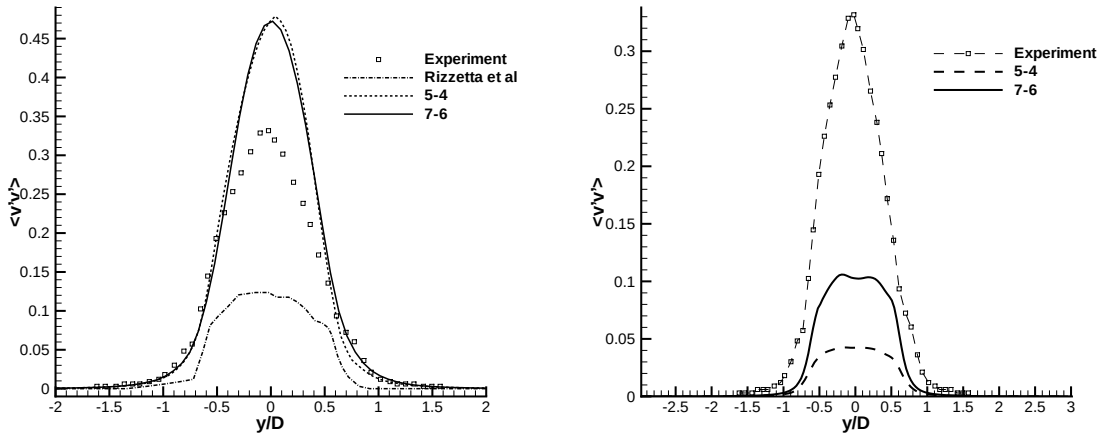

a. $1D$, $120 \times 80 \times 30$ b. πD, $240 \times 160 \times 180$

Figure 8: Lateral Reynolds Stress in the wake at $x/D = 1.54$ Plane

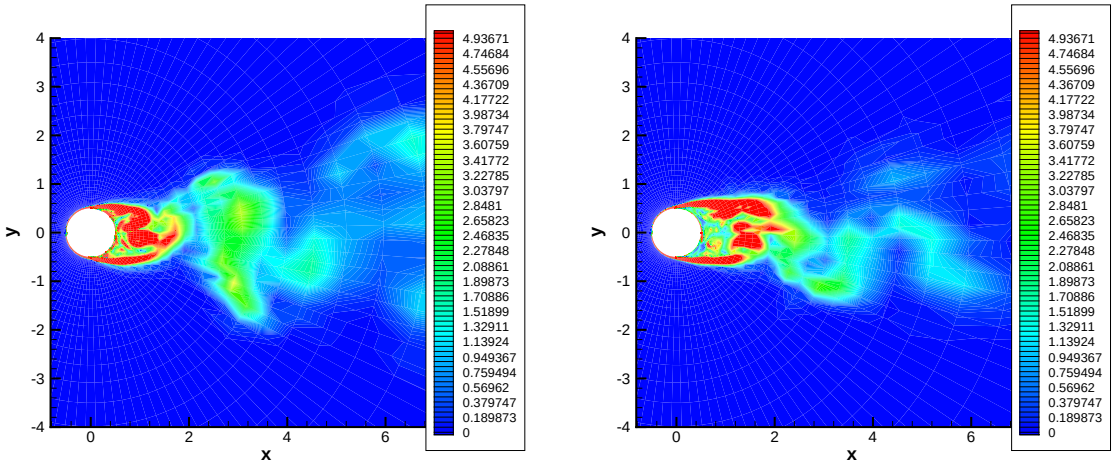

a. 5-4 scheme b. 7-6 scheme

Figure 9: Contours of instantaneous vorticity, t=250T, spanwise length is $1D$, $120 \times 80 \times 30$

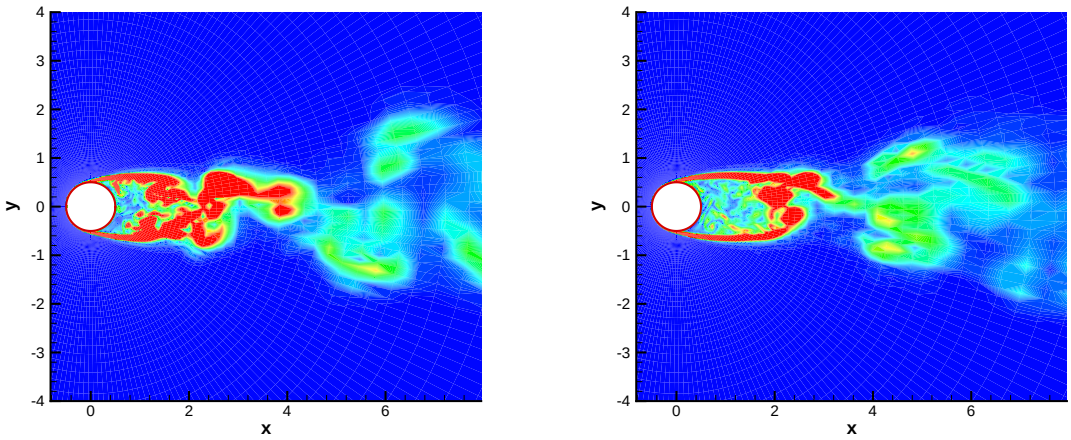

a. 5-4 scheme b. 7-6 scheme

Figure 10: Contours of instantaneous vorticity, t=250T, spanwise length is πD, $240 \times 160 \times 180$